nature geoscience

LETTERS

PUBLISHED ONLINE: 13 JULY 2015 | DOI: 10.1038/NGEO2474

In situ evidence for continental crust on early Mars

V. Sautter[1]*, M. J. Toplis[2], R. C. Wiens[3], A. Cousin[2], C. Fabre[4], O. Gasnault[2], S. Maurice[2], O. Forni[2], J. Lasue[2], A. Ollila[5], J. C. Bridges[6], N. Mangold[7], S. Le Mouélic[8], M. Fisk[9], P.-Y. Meslin[2], P. Beck[9], P. Pinet[2], L. Le Deit[7], W. Rapin[2], E. M. Stolper[10], H. Newsom[11], D. Dyar[12], N. Lanza[3], D. Vaniman[13], S. Clegg[3] and J. J. Wray[14]

Understanding of the geologic evolution of Mars has been greatly improved by recent orbital[1–3], *in situ*[4,5] and meteorite[6–8] data, but insights into the earliest period of Martian magmatism (4.1 to 3.7 billion years ago) remain scarce[9]. The landing site of NASA's Curiosity rover, Gale crater, which formed 3.61 billion years ago[10] within older terrain[11], provides a window into this earliest igneous history. Along its traverse, Curiosity has discovered light-toned rocks that contrast with basaltic samples found in younger regions[12]. Here we present geochemical data and images of 22 specimens analysed by Curiosity that demonstrate that these light-toned materials are feldspar-rich magmatic rocks. The rocks belong to two distinct geochemical types: alkaline compositions containing up to 67 wt% SiO_2 and 14 wt% total alkalis ($Na_2O + K_2O$) with fine-grained to porphyritic textures on the one hand, and coarser-grained textures consistent with quartz diorite and granodiorite on the other hand. Our analysis reveals unexpected magmatic diversity and the widespread presence of silica- and feldspar-rich materials in the vicinity of the landing site at Gale crater. Combined with the identification of feldspar-rich rocks elsewhere[9,13,14] and the low average density of the crust in the Martian southern hemisphere[15], we conclude that silica-rich magmatic rocks may constitute a significant fraction of ancient Martian crust and may be analogous to the earliest continental crust on Earth.

Current understanding of the Martian crust is largely based on orbital spectroscopy[1–4] and meteorite analysis[6–8], which both indicate the predominance of basalts, thought to have formed through partial melting of the mantle. Indeed, the composition of younger Hesperian and Amazonian volcanic terrains is consistent with production of liquids from a mantle that was cooling over time[3]. However, in contrast to the Earth, evidence for significant volumes of deep-seated silica-rich 'continental crust' is lacking on Mars. Localized outcrops of feldspar-rich and silica-rich material have been identified using thermal emission spectroscopy[1,9] and some nearly pure feldspar lithologies have been observed by visible and near-infrared spectroscopy[13,14], although there are inherent challenges in characterizing silicic rocks using these methods. Understanding the petrogenesis of these rocks requires information on their texture, composition and mineral chemistry, which can be obtained only with *in situ* measurements.

The Mars Science Laboratory rover Curiosity landed in Gale crater at the northern edge of the highly cratered Noachian highlands. Curiosity's drive began at the Bradbury landing site, subsequently crossing a distal portion of the alluvial fan derived from Peace Vallis, a fluvial channel cutting through the northern rim of Gale crater (Supplementary Fig. 1a,b). Gale crater is unique with the identification of highly alkaline rocks[16,17], feldspar-rich soils[18] and evidence for feldspar-dominated rocks[19]. Here we focus on leucocratic rocks encountered by Curiosity, concentrating on results from the ChemCam instrument, a laser-induced breakdown spectrometer (LIBS) that provides chemical analyses at a sub-millimetre scale and detailed images with the Remote Micro Imager[20,21] (RMI). Twenty-two light-toned igneous targets have been selected along the traverse (Supplementary Table 1). They are floats within the Hummocky unit (Supplementary Fig. 1b) closely associated with discontinuous conglomerate outcrops (for example, Fig. 1d) of the Peace Vallis system. These rocks have been transported by, and are thus older than, the fluvial system, making them Noachian in age[11]. Their ultimate provenance is a subsurface crustal sequence, several kilometres thick, sampled through the northern wall of the crater.

These light-toned rocks have been grouped into three classes based on crystal textures observed with onboard cameras (Fig. 1).

Group 1 rocks are coarse grained (>5 mm), dominated by leucocratic minerals (~80% of the rock volume: Supplementary Fig. 2b). Rock surfaces vary from flat (Fig. 1a–c) to a knobby appearance (Fig. 1b). Pearly coarse crystals (>5 mm) are locally intergrown with finer (1 mm) rectangular translucent grey grains in a graphic texture (white arrow in Fig. 1a). Anhedral dark grey material forms 20% of the rock (red arrow). Grain sizes and shapes suggest igneous intrusives.

Group 2 samples are vesiculated with conchoidal fractures and shiny scoriaceous surfaces (Fig. 1f). They are largely aphyric at the RMI resolution of 100 μm and they seem to be effusive volcanics.

Group 3 rocks are porphyritic with euhedral, leucocratic phenocrysts up to 2 cm long and 2 mm wide constituting ~50% of rock volume (Supplementary Fig. 2a) embedded in a dark matrix (Fig. 1d,e). These rocks have textures typical of effusive rocks and occur both as float rocks and as clasts (~10 cm in size) in polymict conglomerates (Fig. 1d,e).

Of the 22 samples studied, 11 were selected for their pristine appearance (Supplementary Information). Ninety LIBS measurements on these rocks have been analysed using independent component analysis (Methods). When plotted in an

[1]IMPMC, Muséum d'Histoire Naturelle, 75005 Paris, France. [2]IRAP, 31400 Toulouse, France. [3]Los Alamos National Laboratory, Los Alamos, New Mexico 87545, USA. [4]GeoRessources-Université de Lorraine, 54500 Vandoeuvre les Nancy, France. [5]Chevron Energy Technology Company, Houston, Texas 77056, USA. [6]Space Research Centre, Department of Physics and Astronomy, University of Leicester, LE1 7RH, UK. [7]LPG, BP 92208, 44322 Nantes, France. [8]College of Earth, Ocean, and Atmospheric Sciences, Oregon 97331, USA. [9]Institut de Planétologie et d'Astrophysique, BP 53, F-38041 Grenoble, France. [10]Caltech, Pasadena, California 91125, USA. [11]Institute of Meteoritics, Albuquerque, New Mexico 87106, USA. [12]Mount Holyoke College, South Hadley, Massachusetts 01075, USA. [13]Planetary Science Institute, Tucson, Arizona 85719, USA. [14]Georgia Institute of Technology, Atlanta, Georgia 30332, USA. *e-mail: vsautter@mnhn.fr

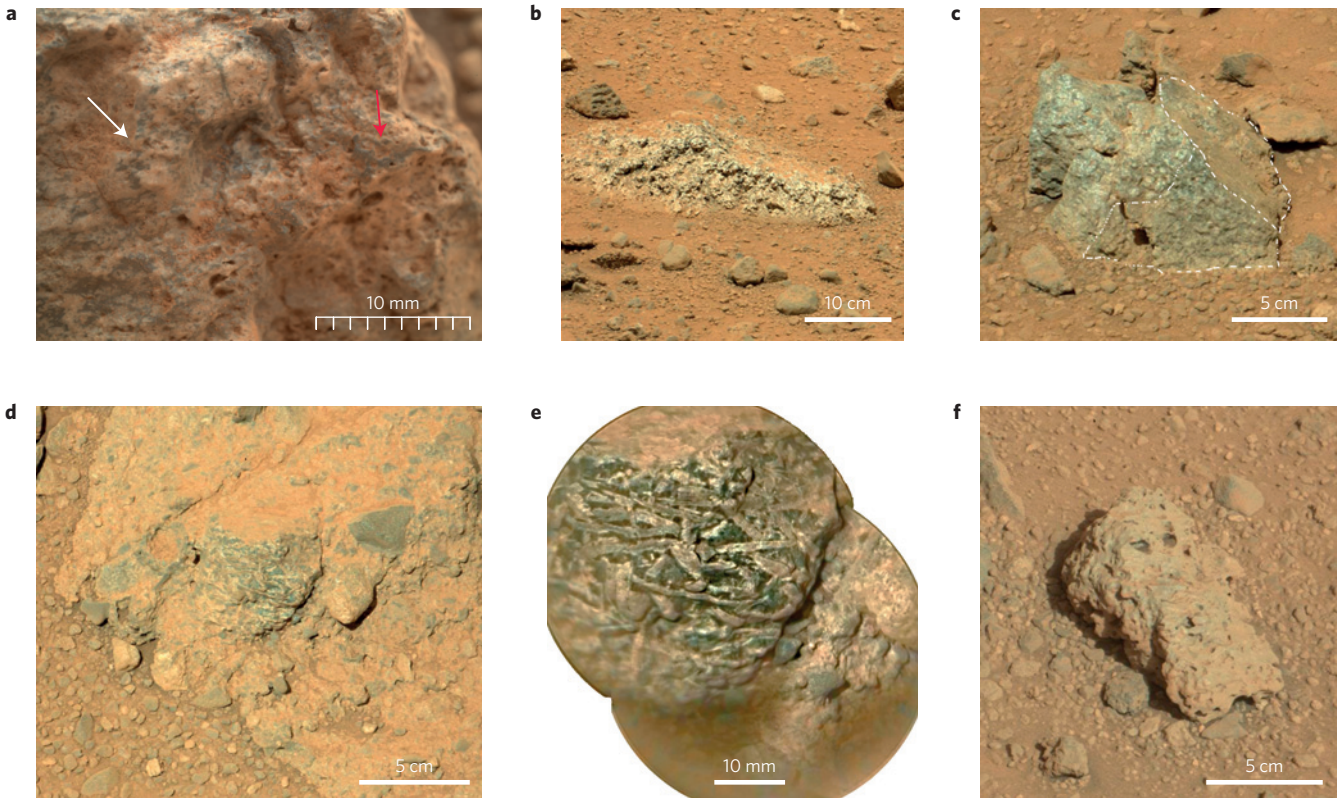

Figure 1 | Diversity of rock textures. a, MaHLI image of Clinton (0512MH0001630000200884R00), showing crystals ~5 mm in size intergrown with greyish translucent 1 mm crystals forming a graphic texture (white arrow). Coarse broken feldspars show fractures filled by darker material (red arrow). **b**, Mastcam image of Little Wind River (0358MR1458000000E1), similar to Bird River, showing the knobby surface of a buried bedrock. **c**, RMI image of Sparkle (0514MR022000000) showing anhedral coarse light-toned crystals. **d**, Mastcam100 image of a polylithic conglomerate including Harrison (centre). **e**, RMI merged with Mastcam showing the igneous clast Harrison, with elongated light-toned crystals embedded in a dark matrix. **f**, Mastcam image of the vesiculated light-toned float rock Becraft (0421MR1726000000E1).

Al versus Si diagram (Fig. 2) with the four silicate-based ChemCam Calibration Targets onboard Curiosity (three synthetic basaltic glasses and a natural 'macusanite' rhyolite[22] with 72% SiO_2 and 16% Al_2O_3) analyses from leucocratic rocks (groups 1 and 2) plot in the Al–Si-rich felsic range. Group 3 rocks plot in the mafic range with the basaltic calibration targets. Some overlap occurs between groups 1 and 3, as both contain a mixture of mafic and felsic materials. Felsic groups 1 and 2 are not as siliceous as the rhyolite calibration target, and Al/Si in the coarse intrusive rocks of group 1 is high. Independent classification using a hierarchical clustering method (Supplementary Fig. 3) leads to identification of three chemical clusters for these 90 individual points. The first is Ca–Al–Si–Sr rich pointing to analyses dominated by plagioclase. The second cluster is rich in K, Al, Si and Ba (Supplementary Table 4) consistent with a K-feldspar component. The third cluster is rich in mafic components and may be subdivided into a Si-bearing, Mg–Ca-rich cluster and a Ti- and Fe-rich one (Supplementary Fig. 3) consistent with mixtures dominated by clinopyroxene and Ti-rich oxides. Further details of the relative proportions of individual phases can be found in the Methods.

Oxide concentrations for each analysis have been quantified using a univariate technique[22] (Methods). In a molar Al/Si versus (Fe + Mg)/Si diagram (Fig. 3 and Supplementary Table 4), LIBS analyses plot along three distinct trends: analyses of felsic intrusives (group 1) define a trend along the y axis from andesine (An ~ 30–45: molar Al/Si of 0.48–0.55) extending towards quartz (Al/Si <0.1 and (Fe + Mg)/Si < 0.2); analyses of felsic effusives (group 2) also plot along the y axis, extending from an Al/Si of alkali-feldspar (Al/Si ≈ 0.33), decreasing to an Al/Si of ~ 0.15; in contrast, LIBS points from porphyritic rocks (group 3) form a clear trend joining oligoclase (An ~ 10–30 with Al/Si 0.37–0.48) and a mafic component with a (Fe + Mg)/Si ratio on the x axis of ~0.5, consistent with an augite-dominated mesostasis.

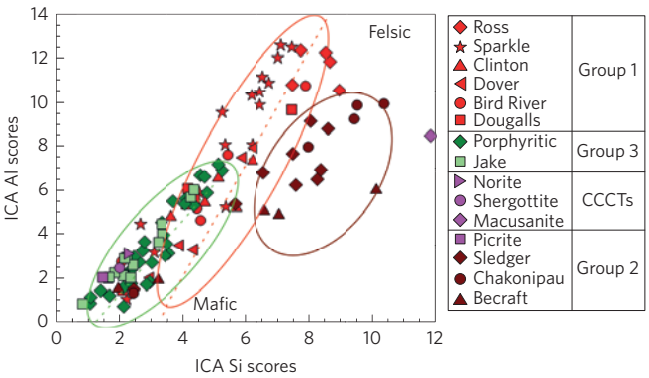

Figure 2 | Independent component analysis diagram in Al versus Si compositional space of the 103 spectra on 11 targets from this study, and Jake-M. x and y axes represent the co-variance between each of the spectra and the independent component. Red symbols are group 1 (coarse intrusives, Fig. 1a–c), brown symbols are group 2 (felsic aphanitic rocks, Fig. 1f) and green symbols are group 3 (porphyritic rocks; Supplementary Table 1). The purple diamond is the rhyolitic macusanite calibration target (37% quartz, 38% albite, and 23% orthoclase), and the other purple symbols are the mafic basaltic calibration targets.

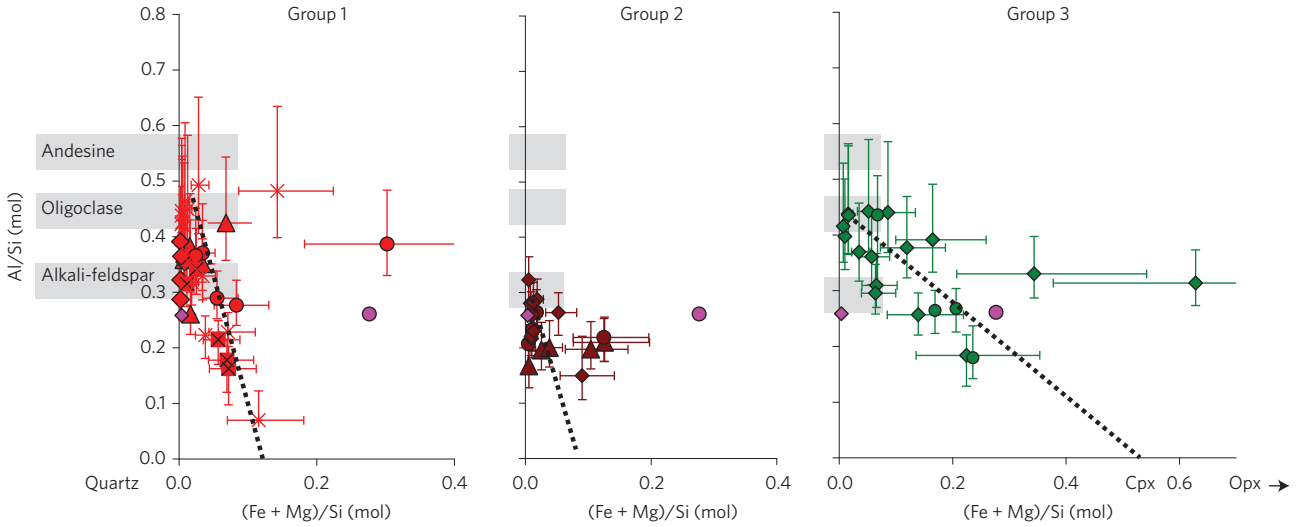

Figure 3 | Element ratio diagrams of Al/Si versus (Fe + Mg)/Si. The diagram includes 90 observation points on the 11 selected targets of this study and two of the onboard calibration targets (macusanite and shergottite glass). Error bars represent the accuracy of the quantification. The compositions plotted in these diagrams are consistent with the presence of plagioclase, alkali-feldspar, and a silica polymorph that all plot on the *y* axis, and augite that plots on the *x* axis. The three different rock groups are indicated using the symbols of Fig. 2 and each group is shown in a separate panel.

Whole-rock compositions for each rock type have been estimated (Methods and Supplementary Table 5). All rocks of group 2, with grain size smaller than the laser beam diameter, have $SiO_2 > 64$ wt% and $Na_2O + K_2O > 10$ wt% consistent with a trachytic composition in total alkali versus silica diagram (Fig. 4). For coarser-grained group 1 rocks, only samples with multi-point rasters were selected to estimate whole-rock composition. The calculated average composition (Supplementary Table 5) has ~64 wt% SiO_2, and $(Na_2O + K_2O) \sim 4.5$ wt%. These rocks are poor in mafic oxides (for example, FeO + MgO + TiO_2 < 12 wt%) and they have an evolved Mg# of ≈0.20–0.30. Normative calculations (Supplementary Table 5) indicate 11–25% quartz, 40–62% plagioclase ($An_{40–49}$), 5–16% orthoclase, 15–21% pyroxene and a calculated density of ~2.8 g cm^{-3}, corresponding to quartz monzodiorite/quartz diorite and granodiorite. The whole-rock compositions of porphyritic group 3 rocks were constrained through a combination of modal proportions (Supplementary Fig. 2b) and compositions of the constituent phases (see Supplementary Fig. 4, Supplementary Table 5 and Methods for details). Calculated compositions plot in the trachyandesite field (Fig. 4) and normative calculations indicate 56% plagioclase ($An_{34}Ab_{65}$), 20% orthoclase, 17% diopside, 6% hypersthene and 0.5% ilmenite. Rocks from groups 2 and 3 define a geochemical trend, from more primitive porphyritic trachyandesite rocks to evolved trachytic samples (Fig. 4).

The bulk composition of igneous rocks observed at Gale, with SiO_2 reaching 67 wt% and $Na_2O + K_2O$ reaching 14 wt%, greatly extends the magmatic diversity observed by lander missions. Although the Mars Exploration Rover Spirit found alkali-rich compositions during its examination of the Noachian terrain in Columbia Hills ($Na_2O + K_2O$ up to 5.5 wt%), those rocks are basaltic with bulk SiO_2 content <52 wt%. Furthermore, they did not exhibit visible feldspar phenocrysts and were interpreted as volcanoclastic tuff[23]. On the other hand, the Martian meteorites NWA_7533 (ref. 7) and NWA_7034 (ref. 8) are Noachian breccias that include millimetre-sized lithic clasts containing andesine, anorthoclase and K-feldspar[7,8] providing independent evidence for early alkali-rich magmatism on Mars, but they are quartz-free.

The generation of alkali-rich parent basalts may be related to low-degree partial melting of the mantle. For example, the compositional trend of groups 2 and 3 is consistent with the 1 bar liquid line of descent for a primary basalt produced by 6% melting at 1 GPa (Fig. 4). Near-surface crystallization of such primary liquids should be associated with low proportions of olivine and high proportions of plagioclase, contrasting with later Hesperian volcanism[12,24], but compatible with terrains of Noachian age[25]. If such alkaline magmatism is indeed a widespread feature of the Noachian, this would challenge the simple idea of continuous cooling of the Martian mantle over geologic time[3], pointing to more complex global or local variations in mantle temperature, for example, associated with the onset or waning of plume-related magmatism.

Our most intriguing finding is the quartz-normative rocks of group 1. Texturally, these rocks are clearly intrusive, originating from a deep-seated unit (quartz diorite/quartz monzonite/granodiorite composition). As such, they differ from andesite (Mars Pathfinder dust-free rock composition[26] in Fig. 4). This unit could be a local pluton, formed through the fractional crystallization of a low-alkali parent. However, we note that quartzo-feldspathic material has also been detected in other distinct locations: ancient uplifted material near the central peaks of craters in the north of Syrtis Major[25]; near the rim of Antoniadi Crater[9]. Furthermore, spectra of the CRISM instrument have shown sporadic feldspar-rich deposits interpreted as either 'anorthosite'[13] or 'granite'[14] in other regions. As orbital detection using visible and near-infrared spectroscopy is capable of identifying feldspar only if the rock is essentially devoid of mafic minerals, these geographically dispersed detections may represent endmembers of more widespread Si-rich intrusive lithologies and it is possible that rocks similar to group 1 samples occur throughout the Martian highlands crust.

Further evidence in favour of this idea is provided by consideration of average crustal density[27]. The density calculated from *in situ* data, Martian meteorites and gamma-ray measurements (>3,100 kg m^{-3}) is considerably higher than the density of the highlands crust constrained by geophysical data[15], a paradox that could be solved by a buried 'light' component in the southern hemisphere[28]. Our observations thus provide the first *in situ* evidence for such a buried crust, while at the same time constraining its petrology.

Class 1 samples are petrologically reminiscent of Archaean trondhjemites, tonalites and granodiorites, some of the Earth's oldest preserved crust[29], and consistent with the interpretation of high-silica material detected from orbit[25]. In detail, we note that the lower

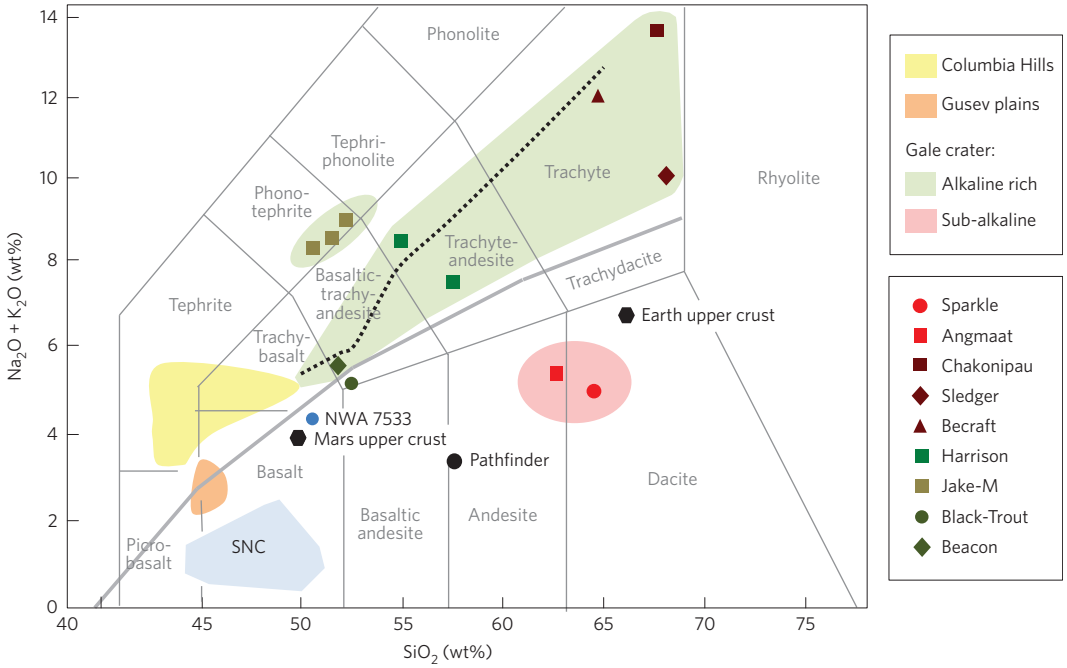

Figure 4 | Total alkali versus silica diagram summarizing the findings of this study. The grey curve indicates the alkaline–subalkaline boundary from ref. 43 (Supplementary Information): Group 1 Ca-felsic intrusive targets (red symbols) plot within the subalkaline field (below the grey curve) and are Si-rich relative to the Pathfinder composition[26]. Group 2 (brown symbols) and 3 (green symbols) are on the alkali field along a common trend starting from trachy-basalt (dark-green symbols; Supplementary Table 5). The dotted black line is a calculated 1 bar fractional crystallization trend of a primary liquid (details in the Methods). The Jake-M alpha-particle X-ray spectroscopy analyses[16] (dark grey squares) are shown for comparison. The SNC blue field includes all Martian meteorites except the Noachian breccia NW7533.

Mg# of the Martian mantle and its higher potassium content relative to the Earth may explain the lower Mg# of our group 1 samples and the absence of tonalite compared with terrestrial samples. Pursuing this analogy, we propose that generation of granodiorite (or rocks slightly poorer in silica such as quartz (monzo-)diorite) could occur through partial melting of pre-existing basaltic crust at relatively low pressure. On early Mars it is possible that dense primitive crust sank into a hot and soft lithosphere leading to partial melting, although further work is required to explore the details of the geodynamical context and the nature of the volatiles required for remelting of primitive mafic crust. An alternative scenario may involve formation of a Martian equivalent of icelandites[30], rocks that have bulk compositions similar to our group 1 samples. Their presence has been previously proposed to explain dust-free silica-rich compositions observed by Pathfinder[26] and they have been suggested as a component of the earliest continental crust on Earth[30]. Independently of their formation process, our data point to the possibility of generating 'continental' crust on Mars, making the early geologic history of Mars much more similar to that of the Earth than acknowledged at present.

Methods

Methods and any associated references are available in the online version of the paper.

Received 28 October 2014; accepted 2 June 2015; published online 13 July 2015

References

1. Christensen, P. R. *et al.* Evidence for magmatic evolution and diversity on Mars from infrared observations. *Nature* **436,** 504–509 (2005).
2. Mustard, J. F. *et al.* Olivine and pyroxene diversity in the crust of Mars. *Science* **307,** 1594–1597 (2005).
3. Baratoux, D. *et al.* Thermal history of Mars inferred from orbital geochemistry of volcanic provinces. *Nature* **472,** 338–341 (2011).
4. McSween, H. Y. *et al.* Elemental composition of the Martian crust. *Science* **324,** 736–739 (2009).
5. Ming, D. W. *et al.* Geochemical properties of rocks and soils in Gusev Crater, Mars: Results of the Alpha Particle X-Ray Spectrometer from Cumberland Ridge to Home plate. *J. Geophys. Res.* **113,** E12S39 (2008).
6. Aouddjehane, H. C. *et al.* Tissint Martian meteorite: A fresh look at the interior, surface, and atmosphere of Mars. *Science* **338,** 785–788 (2012).
7. Humayun, M. *et al.* Origin and age of the earliest Martian crust from meteorite NWA753. *Nature* **503,** 513–516 (2013).
8. Agee, C. B. *et al.* Unique meteorite from early Amazonian Mars: Water-rich basaltic breccia Northwest Africa 7034. *Science* **339,** 780–785 (2013).
9. Bandfield, J. L. Extended surface exposures of granitoid composition in Syrtis Major Mars. *Geophys. Res. Lett.* **33,** L06203 (2006).
10. Le Deit, L. *et al.* Sequence of infilling events in Gale crater, Mars: Results from morphology, stratigraphy, and mineralogy. *J. Geophys. Res.* **118,** 1–35 (2013).
11. Farley, K. A. *et al. In situ* radiometric and exposure age dating of the Martian surface. *Science* **343,** 6169–6174 (2013).
12. McSween, H. Y. *et al.* Characterization and petrologic interpretation of olivine-rich basalts at Gusev Crater, Mars. *J. Geophys. Res.* **111,** E02S10 (2006).
13. Carter, J. & Poulet, F. Ancient plutonic processes on Mars inferred from the detection of possible anorthosite terrains. *Nature Geosci.* **6,** 1008–1012 (2013).
14. Wray, J. *et al.* Prolonged magmatic activity on Mars inferred from the detection of felsic rocks. *Nature Geosci.* **6,** 1013–1018 (2013).
15. Wieczorek, M. A. & Zuber, M. T. The thickness of the Martian crust; Improved constraints from geoid to topography ratios. *J. Geophys. Res.* **109,** E01009 (2004).
16. Stolper, E. M. *et al.* The petrochemistry of Jake_M: A Martian mugearite. *Science* **341,** 6153 (2013).
17. Schmidt, M. E. *et al.* Geochemical diversity in first rocks examined by the Curiosity rover in Gale crater: Evidence for and significance of an alkali and volatile-rich igneous source. *J. Geophys. Res.* **119,** 64–81 (2014).
18. Meslin, P. Y. *et al.* Soil diversity and hydration as observed by ChemCam at Gale crater, Mars. *Science* **341,** 6153 (2013).
19. Sautter, V. *et al.* Igneous mineralogy at Bradbury Rise: The first ChemCam campaign at Gale crater. *J. Geophys. Res.* **119,** 30–46 (2014).
20. Wiens, R. C. *et al.* The ChemCam instruments in the Mars Science Laboratory (MSL) Rover: Body unit and combined system performance. *Space Sci. Rev.* **170,** 167–227 (2012).

21. Maurice, S. *et al.* The ChemCam instruments on Mars Science Laboratory (MSL) Rover: Science objectives and Mast unit. *Space Sci. Rev.* **170,** 95–166 (2012).
22. Fabre, C. *et al. In situ* calibration using univariate analyses based on the onboard ChemCam targets: First prediction of Martian rock and soil compositions. *Spectrochim. Acta B* **99,** 34–51 (2014).
23. Arvidson, R. E. *et al.* Overview of the Spirit Mars Exploration Rover Mission to Gusev Crater: Landing site to Backstay Rock in the Columbia Hills. *J. Geophys. Res.* **111,** E02S01 (2006).
24. Ody, A. *et al.* Global investigation of olivine on Mars: Insights into crust and mantle compositions. *J. Geosphys. Res. Planets* **118,** 234–262 (2013).
25. Bandfield, J. L. *et al.* Identification of quartzofelspathic materials on Mars. *J. Geophys. Res.* **109,** E10009 (2004).
26. McSween, H. Y. *et al.* Chemical, multispectral, and textural constraints on the composition and origin of rocks the Marth Pathfinder landing site. *J. Geophys. Res.* **104,** 8679–8715 (1999).
27. Belleguic, V., Lognonné, P. & Wieczorek, M. A. Constraints on the Martian lithosphere from gravity and topography data. *J. Geophys. Res.* **110,** E11005 (2005).
28. Baratoux, D. *et al.* Petrological constraints on the density of the Martian crust. *J. Geophys. Res.* **119,** 1707–1727 (2014).
29. Moyen, J. F. & Martin, H. Forty years of TTG research. *Lithos* **148,** 312–336 (2012).
30. Reimink, J. *et al.* Earth's earliest continent formed like Iceland. *Nature Geosci.* **7,** 529–532 (2014).

Acknowledgements

The Mars Science Laboratory team is gratefully acknowledged. We would like also to thank D. Baratoux for helpful comments on the manuscript. This research was carried out with financial support from NASA's Mars Exploration Program in the US and in France with the Centre National d'Etudes Spatiales (CNES).

Author contributions

V.S. conceived the manuscript, analysed data, directed the research and wrote the manuscript; M.J.T. conceived and wrote the manuscript; R.C.W. directed the research, and processed the data; A.C., C.F., O.G., S.M., O.F., J.L., A.O., J.C.B. and P.-Y.M. analysed and processed the data; N.M., S.L.M., L.L.D. M.F. and W.R. contributed to interpretation of the data and prepared the figures; E.M.S. contributed to the interpretation and revision of the manuscript; H.N., D.D., N.L., D.V. and S.C. were involved at various stages in data processing; P.P., P.B. and J.J.W. contributed in providing the orbital and *in situ* optical spectroscopic context and related state of knowledge in Martian crustal mineralogy. All authors contributed to the writing and revision of the manuscript.

Additional information

Supplementary information is available in the online version of the paper. Reprints and permissions information is available online at www.nature.com/reprints. Correspondence and requests for materials should be addressed to V.S.

Competing financial interests

The authors declare no competing financial interests.

Methods

Modal estimation from textural analyses. The RMI pixel scale is 19.6 μrad pixel^{-1} (ref. 31) and its spatial resolution with the optimal focus is approximately 2 pixels (ref. 32). The latter gives an idea of the smallest visible grain size, which is relevant for this work. It corresponds to 95 μm at 2.4 m (Clinton, Sledger, Chakonipau, Harrison), and to 140 μm at 3.6 m (Sparkle, Becraft, Horlick).

Modal abundances based on the RMI images of Harrison were analysed with ImageJ 1.47v, which is a software in the public domain and available from the National Institutes of Health of the United States. The RMI image was first converted to a binary image in which feldspar crystals appear in white and dark crystals in black (Supplementary Fig. 2b, right side) and in Supplementary Fig. 2a (Harrison, merged RMI and Mastcam images). Areas of the image were then analysed to determine the percentage of leucocratic material. Three such analyses were performed, one with 10 mm × 10 mm areas and two with 5 mm × 5 mm areas. For the 10 mm × 10 mm analysis, eight non-overlapping areas in two rows were measured across the top part of the porphyritic region of Harrison. For the first group of 5 mm × 5 mm analyses, eleven overlapping areas starting in the upper left of the crystalline area and ending at the lower right edge of the rock were measured. For the second group of 5 mm × 5 mm analyses, thirty-five areas were chosen from four regions of the rock where the contrast between the crystals and matrix was high and where fractures and shadows were not present. Within these four regions each of the thirty-five areas overlapped with a quarter of the area of the images next to them. The average percentage of matrix and the standard deviations of the averages are given in Supplementary Table 2. The crystals, which are brighter than the matrix, make up between 52 and 55% of the rock. The three analyses are the same within 1 s.d., so the surveying method does not seem to have affected the result. The analysis of the thirty-five 5 mm × 5 mm high-contrast regions of the rock provides our best estimate of the percentage of matrix (46%) and light crystals (54%) in Harrison, because it avoided fractures and shadows that were included in the 10 mm × 10 mm survey.

LIBS data processing. Of the 22 samples studied, 11 targets were selected for their pristine mineralogical features and their significant number of chemical analyses. Ninety individual points with 30 laser shots were taken giving a total of 2040 LIBS spectra. These spectra were processed removing the first five shots, which are potentially contaminated by dust, and averaging the remaining 25 spectra. The raw data are processed to remove the noise, the continuum, and the ambient light signal. An instrument response function is corrected for, and the spectra are also corrected in wavelength[33].

Qualitative data processing using independent component analysis (*ICA*). In general terms, the atomic emission line spectrum obtained by ChemCam offers the opportunity to determine compositional variations from small-scale spectral variations. For this purpose, qualitative tools such as hierarchical clustering algorithms[34] and ICA (ref. 35) were first applied using the whole spectral range.

The clustering algorithm is using the ICA components as inputs. We adopt a divisive algorithm[33] that starts with the entire data set followed by iterative binary subdivisions, to search the main data structures. This hierarchical method is also appropriate to find the optimal number of clusters and reveals relations between a parent unit and its sub-units. The schematic dendrogram (Supplementary Fig. 3) presents 5 clusters (A, B, C, D, E). To first order, the analysis distinguishes felsic (A, B, C) from mafic compositions (D, E). The felsic cluster represents 60% of the points classified in this work. On the felsic side, two subclusters are clearly defined: Ca-felsic (A, B) and K-felsic (C) sub-cluster. A1 and B1 boxes in Supplementary Fig. 3 include Ca-felsic targets of group 1 and the core of zoned phenocrysts form group 3 porphyritic targets. B2 is located close to the K-felsic targets of group 2 (C) and is a mixture of K-feldspar and Mg and Fe interstitial matrix. It includes the whitish rim of zoned feldspar phenocrysts in the porphyritic rock Harrison of class 3. Mafic compositions include 45% of observation points in porphyritic rocks (class 3) and correspond to the dark matrix. Slightly less than 20% of the points in coarse intrusive class 1 (red text in Supplementary Fig. 3) are mafic minerals, which are limited in abundance in these light-toned rocks.

ICA is a multivariate analysis technique used to classify components of the spectra[35]. The method produces 'scores' that are linear combinations of the emission peak intensities weighted by 'loading vectors'. The loading vectors for ICA of LIBS spectra have an appearance similar to single-element spectra with strong peaks corresponding to atomic emission lines. ICA has been trained by the ChemCam team to return scores of Si, Ti, Al, Fe, Mg, Ca, Na, K, H and Li for each target point: these scores are monotonic and positive functions of the elemental abundances.

Detailed mineral analysis of Harrison using ICA on shot-to-shot variations in composition with depth is shown in Supplementary Fig. 4. A diagram plotting Na versus K allows Na-feldspar (points 12, 14, 15 and 16) and K-feldspar (points 3, 8) rims to be distinguished. The apatite needle inferred from the Ca–F peak is discussed in ref. 36.

Quantification using univariate data processing. For quantification purposes, we use calibrations based on the onboard ChemCam standards (CCCTs) to infer compositions and elemental ratios[22,33–37]. Elemental compositions were determined from the processed spectra using univariate analysis[22]. Univariate is preferred over multivariate calibration in particular for the felsic targets owing to the lack of sufficient feldspar-rich endmember representation in the multivariate training set[33]. Our analyses used calibrated ratios of spectral emission peaks to provide elemental ratios directly rather than first determining abundances of these elements and then determining the element ratios. In ref. 22 it was shown that univariate calibration curves present good correlation coefficients with low relative standard deviations for major elements for some ratios. Ratios used in this study are Al/Si, (Fe + Mg)/Si, which are discriminators between felsic minerals (Fe-, Mg-free) and mafic minerals (Al-free). They reflect the mineral composition of the rock. Owing to a dearth of high-alkali concentration targets in the CCCT, alkali abundances are estimated using data obtained on Mars with the CCCTs and also on selected Martian fine-grained targets analysed by both alpha-particle X-ray spectroscopy and ChemCam, for which the two instruments showed good agreement for most elements[22].

The accuracy of the quantification values shown in Fig. 4 is calculated using a confidence interval of 95% from calibration curves produced using data from the CCCTs (Supplementary Fig. 5). In detail, the regression line should be applied only for values falling between the lowest and highest reference values. In our case, this is not always possible, especially for high-alkali contents even after adding the alpha-particle X-ray spectroscopy cross-calibration targets. The worst accuracy is for targets with values higher than the CCCT references.

Precision of the technique has been calculated using several data analyses obtained on the shergottite CCCT on Mars[22,37]. This precision is a measure of the reproducibility of the LIBS technique itself. The precision of the measurement has also been evaluated using data from the Sheepbed mudstones, which are homogeneous fined-grained rocks[38]. This precision obtained from Sheepbed targets can be used as an upper limit for the precision in general, as this includes some of the geochemical variations in those targets. In both cases, the precision is given in Supplementary Table 3.

The rationale for Al/Si versus (Fe + Mg)/Si diagram. Such a diagram is useful to distinguish the anhydrous igneous minerals[19]: plagioclase (alkali-anorthite solid solution), nepheline and quartz (or other Si polymorphs) plot on the *y* axis whereas mafic minerals (augite, pigeonite, orthopyroxene and olivine) plot on the *x* axis. Mixtures of pyroxene, olivine and feldspar typical of basalts may therefore be expected to define a three-phase triangle. Increases or decreases in the abundance of one or more minerals result in compositional trends away from an apex of that triangle. For points within these triangles, it is impossible to distinguish chemically a mechanical mixture of different minerals from glassy material with basaltic composition. RMI images are then used to determine the grain size. For anorthite-rich compositions, it is not possible to distinguish nepheline from plagioclase. However, quartz and nepheline being petrologically mutually exclusive, silica-rich rocks cannot contain nepheline. Hydrous mineral phases such as montmorillonite, kaolinite and zeolites also plot on the *y* axis but have not been identified in the present study, where all felsic compositions are hydrogen-poor, that is, anhydrous.

Whole-rock composition estimation. Whole-rock compositions have been estimated for targets with a good sampling, that is, when the crystals are smaller than the laser beam or when at least 9 point analyses have been performed. We were able to calculate the whole-rock composition of a total of seven targets including Black-Trout (Supplementary Table 5). For rocks in group 1, only targets with at least 9 point analyses have been taken into account. For rocks in group 2, WR compositions were obtained by averaging all of the mean spectra obtained for each point analysis for each target. Group 3 rocks are porphyritic and therefore we combined the modal proportions (see Supplementary Fig. 2 and Supplementary Table 2) with the average composition obtained on felsic points (points 12, 14, 14, 16) and mafic ones (points 1, 4, 5, 9, 13). This was possible only for the target Harrison, where two whole-rock calculations have been made, Harrison 1 and 2.

Calculation of liquid line of descent using p-MELTS. The compositional trend described by classes 2 and 3 from Gale crater is compared with a predicted liquid line of descent in Fig. 4. For these calculations (dotted line in Fig. 4), the first step was to calculate primary liquid compositions produced by mantle melting. For this exercise, the p-MELTS thermodynamic calculator was used[39], employing the mantle composition of ref. 40 as a starting composition, assuming an oxygen fugacity 3 log units below the FMQ buffer, and applying corrections to FeO, SiO_2, CaO and Al_2O_3 to account for the Fe-rich nature of the Martian mantle, as described in refs 3,41. Simulations were performed at 1, 1.5 and 2 GPa for degrees of partial melting from 3 to 30%. Fractional crystallization of these primary liquids was then simulated at a pressure of 1 bar and an oxygen fugacity 3 log units below the FMQ buffer using the MELTS software[39]. The best fit to the compositional

trend described by classes 2 and 3 from Gale crater is found for fractionated liquids of primary melts produced at 1 GPa for degrees of partial melting of the order of 6%, as illustrated in Fig. 4. Micro gabbro (Beacon and Black-Trout[42]) have been included (Supplementary Table 5) as the mafic endmember of the calculated liquid line. The alkaline–subalkaline boundary curve in Fig. 4 is from ref. 43.

References

31. Le Mouélic, S. *et al.* The ChemCam remote micro-imager at Gale crater: Review of the first year of operations on Mars. *Icarus* **249,** 93–107 (2014).
32. Langevin, Y. *et al. Processing Approaches for Optimal Science Exploitation of the ChemCam Remote Microscopic Imager (RMI) During the First 90 Days of Curiosity Operations* in *44th Lunar Planet. Sci. Conf.* Abstract 1227 (Lunar and Planetary Institute, 2013).
33. Wiens, R. C. *et al.* Pre-flight calibration and initial data processing for the ChemCam laser-induced breakdown spectroscopy instrument on the Mars Science Laboratory rover. *Spectrochim. Acta B* **82,** 1–27 (2013).
34. Gasnault, O. *et al. ChemCam Target Classification: Who's Who from Curiosity's First Ninety Sols* in *44th Lunar Planet. Sci. Conf.* Abstract 1994 (Lunar and Planetary Institute, 2013).
35. Forni, O. *et al.* Independent component analysis classification of laser induced breakdown spectroscopy spectra. *Spectrochim. Acta B* **86,** 31–41 (2013).
36. Forni, O. *et al.* First detection of fluorine on Mars: Implications for Gale Crater's geochemistry. *Geophys. Res. Lett.* **42,** 1020–1028 (2015).
37. Fabre, C. *et al.* On board calibration targets for the MSL/ ChemCam LIBS instrument. *Spectrochim. Acta B* **66,** 280–289 (2011).
38. Blaney, D. *et al.* Chemistry and Texture of the rocks at Rocknest, Gale crater: Evidence for sedimentary origin and diagenetic alteration. *J. Geophys. Res.* **119,** 2109–2131 (2015).
39. Ghiorso, M. S. *et al.* The pMELTS: A revision of MELTS aimed at improving calculation of phase relations and major element partitioning involved in partial melting of the mantle at pressures up to 3 GPa. *Geochem. Geophys. Geosyst.* **3,** 1030–1038 (2002).
40. Dreibus, G. & Wanke, H. Mars, a volatile rich planet. *Meteoritics* **20,** 367–381 (1986).
41. Ghiorso, M. S. & Sack, R. O. Chemical mass transfer in magmatic processes. iv. a revised and internally consistent thermodynamic model for the interpolation and extrapolation of liquid–solid equilibria in magmatic systems at elevated temperatures and pressures. *Contrib. Mineral. Petrol.* **119,** 197–212 (1995).
42. Cousin, A. *et al. Igneous Rock Classification at Gale (Sols 13–800)* in *46th Lunar Planet. Sci. Conf.* Abstract 2452 (Lunar and Planetary Institute, 2015).
43. Irvine, T. N. & Baragar, W. R. A. A guide to the chemical classification of the common volcanic rocks. *Can. J. Earth Sci.* **8,** 523–548 (1971).